ARTICLES

Predissociation and Vibrational Relaxation in the B State of I_2 in a Kr Matrix

M. Gühr, M. Bargheer, P. Dietrich, and N. Schwentner*

Institut für Experimentalphysik, Freie Universität Berlin, Arnimallee 14, 14195 Berlin, Germany

Received: January 30, 2002; In Final Form: August 14, 2002

An apparent predissociation rate k_{pre} of 0.06 ps^{-1} at 10 K which rises to 0.11 ps^{-1} at 40 K is observed in pump−probe spectra of the population arriving in predissociated states. We show that the observed rate is determined by a balance of the calculated energy-dependent predissociation rate $k_p(E)$, which rises in approaching the relevant curve crossing from higher energies, and the vibrational relaxation rate k_{vib}, which funnels population toward this crossing. k_{vib} is explored via several probe windows using fluorescence emitted by three different ionic states. k_{vib} increases exponentially with energy above the B state potential minimum. Predissociation occurs in a region where k_{vib} equals k_p. The increase of k_{vib} with matrix temperature T explains the rise of k_{pre} at 40 K. Disorder induced by double doping furthermore increases k_{vib}. The deduced effective curve crossing matrix element of 15−20 cm^{-1} is in accordance with calculations.

1. Introduction

The central problem in chemical dynamics, how a reaction proceeds from reactants to products, is tackled on the multidimensional potential energy surfaces present in the condensed phase by ultra-short-time spectroscopy with increasing success. Studies on small molecules in solid and liquid rare gases play a major role in bridging the gap between experiments and theoretical modeling. The photoinduced dissociation and recombination of I_2 in solution has been considered as a prototype for the solvent cage effect since the work of Rabinovitch and Franck.[1] The relevant time scales for geminate recombination and vibrational relaxation in the ground state are summarized in the excellent review by Harris et al.[2] The incompletely resolved issues on the medium-induced predissociation which must occur prior to geminate recombination were treated in a seminal series of experiments in the group of Zewail. Combining the results from the dilute gas phase up to densities of the liquid phase,[3−5] they derived a unifying relation for a reduced predissociation rate which was confirmed for all four rare gases.[3] It predicts a linear increase of the predissociation rate in the B state with density. Rates of about 1 ps^{-1} are obtained for Ar at the supercritical density, and somewhat larger rates are predicted for Kr (k_{exp}(300 K) in Figure 1). Even shorter predissociation times on the order of 200−400 fs were reported for more complex solvents such as *n*-hexane[6] and CCl_4.[7] However, the Apkarian group observed a predissociation probability in a Kr matrix nearly an order of magnitude smaller than in the liquid phase (k_{exp}(15 K) in Figure 1), while the local density nearly doubles in the solid compared to the liquid.[8] This systematic decrease of the curve crossing probability in the predissociation process from the disordered liquid to the ordered solid environment was confirmed in a study devoted to this effect.[7] The decrease of probability was attributed to a cancellation effect in the summation of the angular terms of the nonradiative matrix elements due to the higher symmetry of the crystalline surroundings.

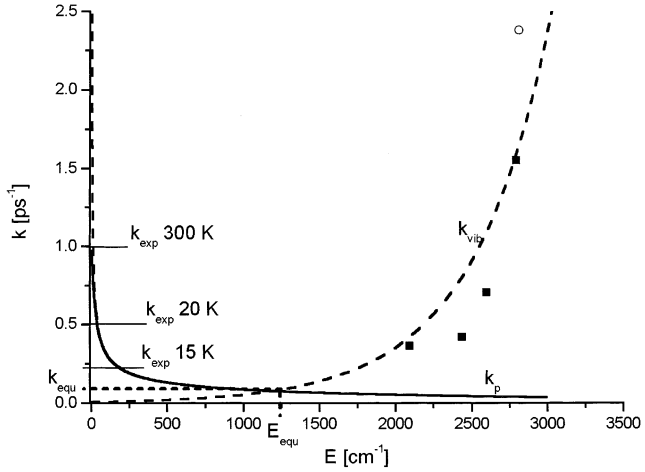

Figure 1. Predissociation rate k_p calculated according to eqs 1−3 (dashed line) and ref 20 (solid line) both with V_{a-B} = 30 cm^{-1}.[11] Vibrational relaxation rate k_{vib} in solid Kr from experiments (squares[9]), calculations (circle[8]), and exponential extrapolation (dashed line). The crossing of k_p and k_{vib} defines k_{equ} and E_{equ} according to the text. Experimental predissociation rates near the liquid phase at 300 K[3] and in the matrix at 20 K[9] and 15 K[8] are indicated by horizontal lines.

A predissociation time in solid Kr of 2 ps (k_{exp}(20 K) in Figure 1) reported in ref 9 is about a factor of 2 shorter than the corresponding value in ref 8, but nevertheless, it is in accordance with a decrease of the predissociation rate in the solid matrix with respect to the liquid. Finally predissociation times of 4.5 ± 1.5 ps were derived for solid Xe, Kr, and Ar from hot luminescence in the B → X emission in combination with a

* To whom correspondence should be addressed. E-mail: nikolaus.schwentner@physik.fu-berlin.de.

10.1021/jp0202993 CCC: $22.00
Published on Web 11/20/2002

classical simulation of vibrational energy relaxation in the B state, a result in agreement with the time-resolved studies.[10]

Treating caging and predissociation in van der Waals complexes, Roncero, Halberstadt, and Beswick[11] derived the angular dependence of the electrostatic coupling between the B state and the crossing a($^3\Pi_g$) state used in ref 7. While coupling to other crossing states may be present, it is this B−a coupling which seems to dominate at least at low densities. From comparison with experiment, values of 30 cm^{-1} [12] and 14 cm^{-1} [11] are considered for the electronic part of the B−a coupling matrix element. Ben-Nun, Levine, and Fleming[13] simulated the wave packet dynamics in liquid Xe, Kr, and Ar for an electrostatic coupling between the B and a states in close relation to the experiments of Scherer et al.[6] They obtain a monotonic increase of the predissociation probability with density. The restriction on coupling to the a state alone was eliminated in an ambitious effort by Batista and Coker. They use a semiempirical diatomic-in-molecules Hamiltonian and propagate trajectories on 23 nonadiabatically coupled states for liquid Xe[14] and also for solid Ar and Xe.[15] A similar Hamiltonian was applied to I_2−Ar by Buchachenko and Stepanev.[16] These simulations lead to a strong coupling of the B state to a variety of crossing states and to very rapid predissociation in accordance with the liquid-phase results. However, they do not reproduce the significantly slower predissociation in the solid phase. Therefore, the surface hopping approach was reconsidered and improved in a recent calculation.[17] The evaluation attempted to resolve the liquid−solid-phase issue. Indeed, the calculated B state pump−probe signal for I_2 in liquid Xe reproduced the measured decay of the B state in liquid CCl_4. In addition to this, the calculations delivered B state signals persistent for 3 ps in solid Ar. The main channel for predissociation was attributed to a B−a′($^3\Pi_{2g}$) transition, in which the coupling matrix element is symmetric with respect to the angle of the I_2 bond vector and vector to a matrix atom. A cancellation of terms from cage atoms placed symmetrically on both ends of the molecular axis occurs in the ordered solid and is weakened in the disordered liquid. This is considered as the dominant reason for the increase of the dissociation rate in the liquid compared to the solid phase. However, the nonradiative transition rate also decreases strongly with increasing energy above the avoided crossing.[18] The vibrational wave packets in the solid phase are prepared high above the crossing. Vibrational relaxation will move the wave packet closer to the crossing point and thus increase the predissociation rate. An increase of the vibrational relaxation rates from the solid to the liquid phase would also contribute to an increase of the B state predissociation in the liquid phase. This aspect is contained in the calculations,[17] but was not extracted explicitly.

In another recent simulation of pump−probe spectra for the case of I_2 in high-pressure Ar by a classical molecular dynamics calculation, this strong connection between vibrational relaxation and predissociation was reemphasized,[19] and deviations from a single-exponential decay were explained by the combination of both processes.

In this paper we focus on the connection between vibrational energy relaxation within the B state and the rate of predissociation from the B state to crossing states. This interrelation is worked out in a model presented in section 2 together with the available theoretical and experimental data. The survey indicates that for the solid matrixes measurements of vibrational energy relaxation rates closer to the curve crossing are desirable and in addition direct measurements of the predissociation rates are necessary. Therefore, the spectroscopic limitations are illustrated in section 4, and vibrational energy relaxation rates are determined in section 5. The explicit explanation at hand up to now for the reduced predissociation rates in the solid phase is based on the cancellation effects in the matrix elements of curve crossing for an environment of high symmetry.[7] Therefore, we gradually reduce the symmetry of the solid matrix by temperature-induced disorder and by adding statistically an atom of different size (Ar) to the shell of next-nearest neighbors (Kr). We determine the vibrational relaxation (section 5) and the predissociation rates (section 6) separately. The combined discussion in section 7 indicates that a variation of the vibrational relaxation rate with environment initiates strong changes in the predissociation rates.

2. Model and Available Data

Figure 1 shows the recent experimentally determined vibrational relaxation rate constants $k_{vib}(E)$ versus the energy E above the bottom of the B state.[9] The experiments deliver an energy relaxation rate k_{en} in cm^{-1}/ps. The vibrational energy $h\nu_{osc}$ in the B state in this range is available from the determined anharmonicity and corresponds to about 120 cm^{-1}. Thus, the lifetime of a vibrational level, i.e., the time until the energy difference to the next lower vibrational level is dissipated, is given by $h\nu_{osc}/k_{en}$, and its inverse is taken as the vibrational relaxation rate k_{vib} in Figure 1. Also included is the value from the recent classical trajectory calculation for solid Kr[8] which was adopted in the same way. The calculations for liquid Xe[10] show that k_{vib} decreases with decreasing E in a way similar to that of the experimental results for Kr. Obviously k_{vib} decreases strongly and monotonically with decreasing E. Unfortunately there is a gap between $E = 0$ cm^{-1} and $E = 2000$ cm^{-1} which will be addressed in sections 3 and 4. A smooth extrapolation (dashed line) would suggest a further decrease.

This work continues a series of experimental and theoretical investigations on B state predissociation in diluted gas and condensed phases. The common theme of all these investigations is that predissociation occurs in the I_2 potential energy surfaces and is therefore predetermined by the crossings of the B state with repulsive I_2 surfaces (B″($^1\Pi_{1u}$), a(1g), a′(2g)). The coupling to the repulsive surfaces in the free molecule is weak due to symmetry reasons. The coupling is modified by the interaction with predissociation-enhancing surroundings. The predissociation rate is therefore considered as a product of two terms.

The first contains the Frank−Condon factors for the B state and the relevant crossing state which can be calculated explicitly[11,12] or handled classically as in the Landau−Zener scheme and in the trajectories.[8] We follow the Landau−Zener scheme in its quantum mechanical analogue given by Nakamura.[20,21]

The second term describes the coupling of the I_2 surfaces due to the interaction with the surroundings. The couplings are derived in DIM and DIIS simulations explicitly and are given by nonadiabatic matrix elements V_{x-B}.[14,15] The matrix elements show up with the same meaning in the Landau−Zener or Nakamura expressions.

Per se, this matrix element can be sensitive to several coordinates, and the appropriate description would then be a multidimensional coupling of the B state with a predissociating state. The previous and present experiments monitor the internuclear coordinate of I_2, and the couplings are therefore combined in an effective coupling matrix element. The coupling can then depend on local structure, which is the central issue of the cancellation model for the solid−liquid effect, and on

the population of the lattice modes. Therefore, we also introduce this effective coupling matrix element V_{x-B} and study its dependence on local structure (codoping the Kr matrix with Ar) and temperature.

The curve crossing between B and the predissociating states ($B''(^1\Pi_{1u})$, a(1g), a′(2g)) is situated within one vibrational level, i.e., within ~100 cm^{-1} above the bottom of the B state in the gas phase. For convenience we place the dominant crossing at $E = 0$ in Figure 1 since it will turn out that the energetics are not better defined. The standard expression for the curve crossing probability p_{LZ} is given by

$$p_{LZ} = 1 - \exp\left(-\frac{A}{E^{1/2}}\right) \quad (1)$$

according to the semiclassical derivation by Landau−Zener (refs 18 and 22). The term $1/E^{1/2}$ arrives from the velocity above the crossing point. The crossing point is passed twice in each round trip of a wave packet.[13] The rate k_p is calculated for small p_{LZ} by

$$k_p = -c\hbar\omega_v \ln(1 - 2p_{LZ}) \quad (2)$$

with

$$A = \frac{\sqrt{2\mu}\pi V^2_{a-B}}{\hbar|F_a - F_B|} \quad (3)$$

For a numerical illustration we use the well-characterized a−B crossing. In this case, A is determined by the electronic coupling matrix element V_{a-B} and the difference in the forces F_a and F_B on the potential surfaces a and B in the crossing point and the reduced mass μ. Using the cited values of 30 cm^{-1} [12] and the literature data for F_a and F_B,[23] we obtain the dashed line for k_p given in Figure 1.

The classical probability p_{LZ} in eq 1 goes to unity for $E \rightarrow 0$, and we have to introduce the quantum mechanical probability derived by Nakamura et al.[20,21] Equations 3.25a and 3.25b in ref 20 and the same input data yield the solid line for k_p.

The resulting k_p values are very similar. Only near $E = 0$ the quantum mechanical rates are smaller and remain finite. k_p increases strongly with decreasing E, and for the chosen parameters we obtain a maximal value k_p^{max} of about 1 ps^{-1}. Obviously the dependence of k_p on E is just inverse that of k_{vib}. Suppose a vibrational population is prepared by a short pulse at large energies $E > 2000$ cm^{-1}. This population will quickly relax in energy due to the large k_{vib}, and very little population will be lost because the competing k_p is much smaller. At lower E the vibrational relaxation slows down, and the situation changes completely if the population has reached an energy around E_{equ} where the $k_p(E)$ and $k_{vib}(E)$ curves cross with an equal rate k_{equ}. At E_{equ} a great part of the population in the B state which has reached this point will be lost within the vibrational lifetime by predissociation (here to the a state). The small population surviving in the B state at energies below E_{equ} will be damped even faster. The rate k_{equ} can be determined by measuring the predissociating population dynamics. This scheme in Figure 1 illustrates that the predissociation process includes an energy relaxation cascade which will lead in general to a deviation from a single-exponential decay.[19] The discussion will show the connection between k_{equ} and the average and effective predissociation rate k_{pre} seen in the experiments. Now from Figure 1 it is obvious that an enlarged $k_{vib}(E)$ will shift k_{equ} to larger rates despite the fact that $k_p(E)$ may have been the same. Thus, a faster vibrational relaxation leads to a higher apparent predissociation rate even if the underlying matrix elements for curve crossing remain unchanged. Of course an increase in $k_p(E)$ also shifts k_{equ} to larger values with an apparent increase in the predissociation rate. To resolve this interplay, it is essential to separate k_{vib} and k_{equ}. In this way the origin of the difference of the predissociation rates in the solid and liquid phases may also be singled out.

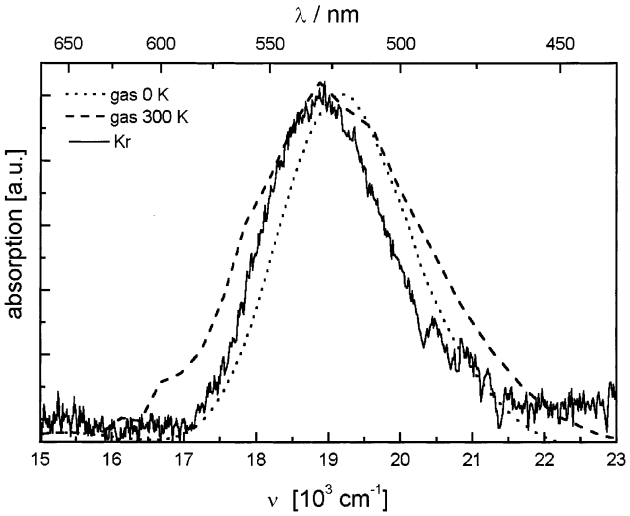

Figure 2. Measured absorption spectrum in Kr at 20 K (solid line) compared to the gas-phase Franck−Condon envelope at 300 K (dashed line[27]) and the calculated one at 0 K (dotted line).

3. Experiment

The samples consisting of 30 μm thick clear crack-free films of Kr doped with I_2 in a ratio of 1000:1 were prepared in the same way as described in ref 9. The fluorescence around 420 nm consists of three contributions.[24] The spectroscopy and the separation of these bands are essential because they provide different dynamics in the pump−probe spectra. Therefore, the fluorescence was dispersed by a double monochromator (0.25 m, B&M Spektronik) and recorded by a photomultiplier. In this way variations in the spectral distribution with temperature and with time delay to the exciting pulse were investigated. Stray light rejection was accomplished by appropriate long-pass and band-pass filters. The pump beam used to excite the B state was tuned from 600 to 480 nm, and the probe wavelength was tuned between 550 and 456 nm. Our laser system consists of a commercial CPA 2001 and two noncollinearly pumped optical parametric amplifiers (NOPAs).[25] A more detailed description with an improvement in the NOPA pumping optics is presented in ref 26. Alternatively the second harmonic of the Ti Sa laser at 387.5 nm with a pulse width of 150 fs was used for probing. The pulses are characterized by autocorrelation and cross-correlation. Absorption measurements were carried out with a high-pressure Xe lamp in standard transmission geometry and with optical multichannel detection.

4. Absorption and Fluorescence Spectra

The measured absorption spectrum of I_2 in Kr (Figure 2) can be decomposed into the hardly visible transition to the A state (600−700 nm), the strong transition to the B state (600−500 nm), and the overlapping transition to the B″ state (520−450 nm) according to the standard assignment.[27] No vibrational structure is resolved in the matrix due to the strong dephasing of bath modes.[10,28] The spectrum reported by Grzybowski and Andrews[29] for Ar is very similar for $\lambda > 530$ nm but has a

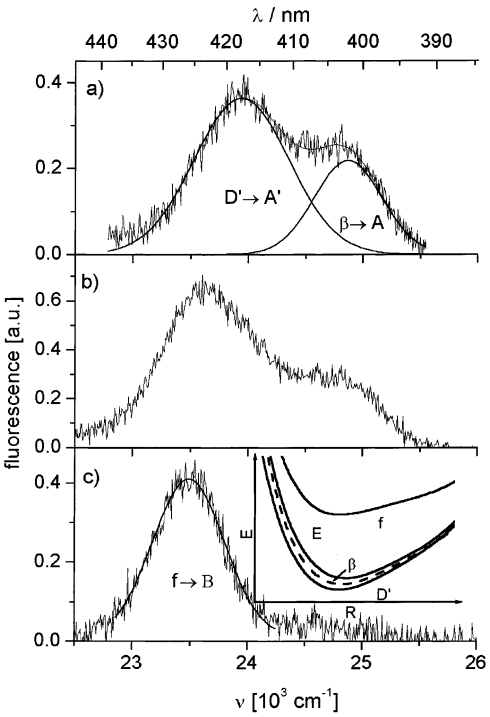

Figure 3. Fluorescence spectra in Kr at 20 K for $\lambda_{pump} = 560$ nm and $\lambda_{probe} = 336$ nm. (a) A time delay of ~1 ms yields two bands at 418 and 402 nm assigned to D′ → A′ and β → A (according to ref 24, perhaps δ → A) transitions. (b) A short time delay (500 fs) leads to an additional band at 426 nm which is isolated in (c) by subtraction of (a) from (b). It is assigned to an f → B transition according to the scheme of ionic states in the inset.

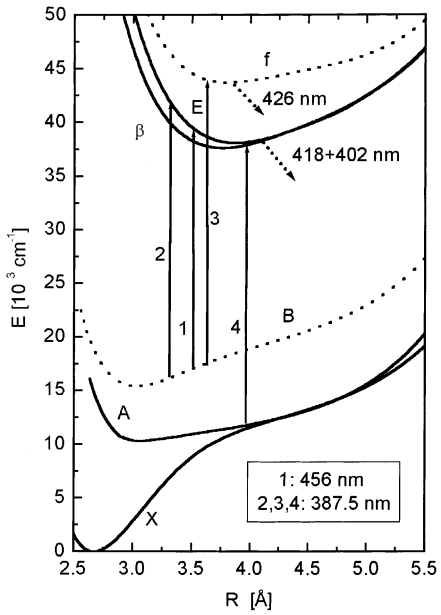

Figure 4. Scheme of probe windows to detect vibrational relaxation (1−3) and predissociation (4). $\lambda_{probe} = 456$ nm determines window 1. $\lambda_{probe} = 387.5$ nm yields windows 2−4. Window 3 is distinguished from windows 2 and 4 by a different fluorescence band at 426 nm (see Figure 3).

TABLE 1: Energy *V* and fwhm Δ*V* of the Fluorescence Bands in Figure 2

V (cm^{-1})	ΔV (cm^{-1})	
23940	959	D → A
24870	685	β → A or δ → A
23489	719	f → B

somewhat more pronounced blue wing around 520 nm. A comparison with the gas-phase Franck−Condon envelope measured at room temperature ($T = 300$ K)[27] shows a long red wing for the free molecule. It originates from thermal population of $v = 1$ and $v = 2$ in the electronic ground state according to the comparison with our calculated spectrum for $T = 0$ K, i.e., only the $v = 0$ population in Figure 2. The matrix and the $T = 0$ K gas spectra have rather similar shapes. The red shift of the maximum in the matrix originates from a smaller $T_e = 15420$ cm^{-1} compared to the gas-phase value of $T_e = 15769$ cm^{-1},[30] which has been worked out in a detailed spectroscopic investigation of the B state in Kr.[31]

According to Figure 1 it would be important to close the gap in the experimental k_{vib} value between E = 0 cm^{-1} and $E = 2000$ cm^{-1}. However, the B state absorption in Kr is too weak to allow for an excitation for $\lambda > 590$ nm, which corresponds already to an E value of 1550 cm^{-1}. The long red wing in the gas phase at 300 K and the larger T_e support an excitation at small E. Indeed the investigations by Zewail were carried out at 620 nm and E values of about 400 cm^{-1}. If an excitation in the matrix at $\lambda > 600$ nm is attempted, then the spectra are dominated by the underlying stronger A state contributions as shown in section 5.

Since direct pumping in this energy range is not feasible, it is desirable to search for probe transitions which sample the bottom region of the B state. The fluorescence spectrum between 400 and 450 nm was investigated by a variety of pump and probe wavelength combinations at variable delays and different sample temperatures. The results are summarized in Figure 3 for a pump wavelength of 560 nm, i.e., in the center of the B state transition and a probe wavelength of 336 nm, which is short enough to reach several branches in the ionic manifold. For a long delay of about 1 ms the population is relaxed to the A and A′ states. Then only the lower ionic manifold can be reached, and two bands with wavelengths of 418 and 402 nm are observed (Figure 3a). The assignment of the long-wavelength band to emission from the lowest state D′ is obvious, and from selection rules the D′−A′ transition is favored. Accordingly the band at 402 nm could be attributed to the next-higher state β with a β−A transition, but in ref 24 an assignment to δ−A is suggested by a rather detailed analysis. For a short delay (here 500 fs) the population in the B state can also be probed to the second ionic manifold, and an additional band at longer wavelength shows up in Figure 3b. Subtraction isolates this band (Figure 3c), which has a wavelength of 426 nm and belongs to the f−B transition (see the inset in Figure 3). The parameters from a Gaussian deconvolution are collected in Table 1. The spectroscopic data and also the temperature effects are in full agreement with ref 24, and for a detailed discussion of matrix effects we refer to this work.

Figure 4 summarizes the relevant electronic states and illustrates the strategy for the probe wavelength choice. It should avoid the region from 400 to 450 nm to allow for stray light rejection. To single out dynamics in the B state, it should be longer than 400 nm to avoid competing A state excitation, and it should be as short as possible to reach the bottom of the B state. Therefore, we use a probe wavelength $\lambda_{probe} = 456$ nm for this purpose. The probe window (1) for this wavelength lies at the turning point of a wave packet pumped with 580 nm. This probe window is located at an I−I internuclear distance of $R = 0.35$ nm and an energy $E = 1690$ cm^{-1} above the bottom of the B state as detailed in ref 31 and corresponds to the lowest energy in the B state that can be probed with good stray light suppression and without probing the A state.

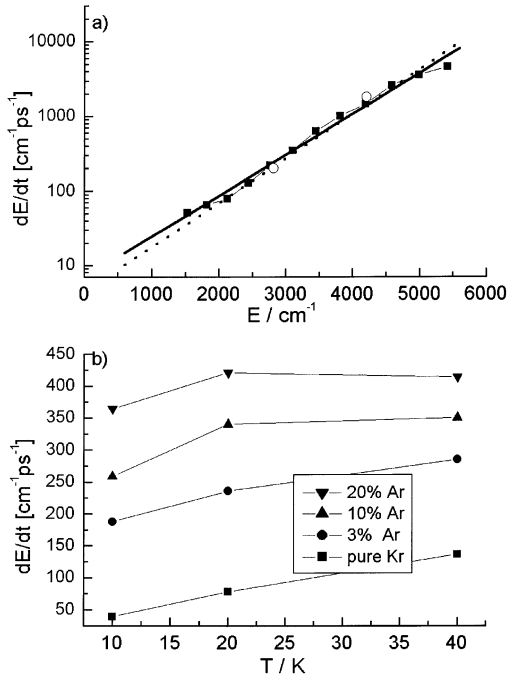

Figure 5. (a) Vibrational energy relaxation rate $k_{en} = dE/dt$ at 20 K in solid Kr versus energy E above the B state minimum (squares) compared to calculation[8] (circles). Best fit (solid line) and lower limit (dotted line) for exponential energy dependence. (b) dE/dt versus temperature T with values in pure Kr (squares) and 3%, 10%, and 20% Ar codoping at 10, 20, and 40 K. The dE/dt values are given at about 2000 cm^{-1} above the B state minimum.

$\lambda_{probe} = 387.5$ nm results in three probe windows (2−4). Window 2 probes the B state at $R = 0.33$ nm close to its minimum and at $E = 700$ cm^{-1}; probe window 3 is at 0.36 nm in the B state, which leads to the second ionic manifold. It can be distinguished via the fluorescence wavelength of 426 nm. Finally $\lambda_{probe} = 387.5$ nm probes the A state population to the lowest ionic manifold (window 4). This transition is stronger than that of window 2 but yields the same fluorescence. Therefore, this wavelength will be used to probe the population after predissociation and thus the depopulation dynamics of the B state.

5. Vibrational Relaxation in the B State

The vibrational relaxation funnels a wave packet prepared at energy E down to lower energies, and in the time course of a pump probe spectrum a shortening of the oscillation periods (i.e., an increase in vibrational frequency ν) appears because the wave packet reaches regions of larger vibrational spacings according to the anharmonicity in a Morse-like potential. The derivation of $d\nu/dt$ values from the time course is discussed in detail in refs 9 and 31. The first oscillation period for a variation of the pump energy yields the oscillation frequency $\nu(E)$ versus the energy above the B state bottom and from this the anharmonicity $d\nu/dE$. Combining $(d\nu/dE)^{-1}$ and $d\nu/dt$ provides us with the energy relaxation rate $k_{en} = dE/dt$ in cm^{-1}/ps according to ref 9. We extended the pump wavelength range to the long-wavelength limit of 600 nm (Figure 5) and included shorter wavelengths down to 500 nm. In addition we observed that the probe wavelength has to be optimized systematically for obtaining accurate $\nu(E)$ and $d\nu/dt$ values.[31] The evaluation is discussed in more detail in ref 9. The improved values of k_{en} are approximately 30% larger at low energies and shown as squares in Figure 5a. They are converted to vibrational relaxation rates k_{vib} as described in section 2.

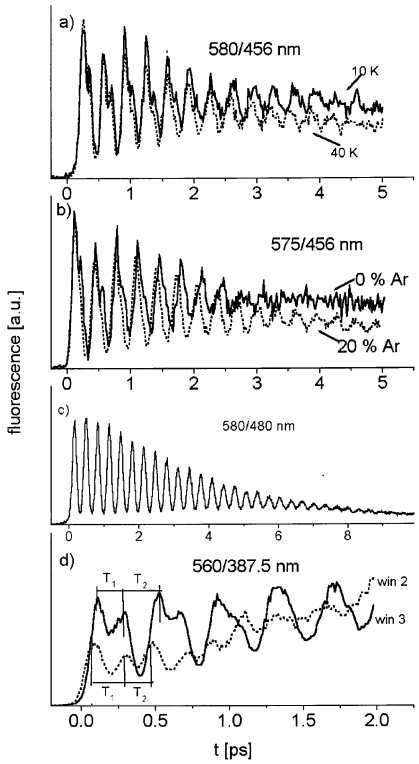

Figure 6. Fluorescence intensity versus time delay between the pump pulse with wavelength λ_{pump} and probe pulse with wavelength λ_{probe}. (a) Comparison between $T = 10$ K (solid line) and $T = 40$ K (dashed line) for pure Kr, $\lambda_{pump} = 580$ nm, and $\lambda_{probe} = 456$ nm. (b) Comparison between pure Kr matrix (solid line) and additional doping with 20% Ar (dashed line) for $\lambda_{pump} = 575$ nm and $\lambda_{probe} = 456$ nm. (c) Variation in pure Kr with longer $\lambda_{probe} = 480$ nm (same $\lambda_{pump} = 580$ nm) at $T = 10$ K to be compared with (a). (d) Dynamics monitored by windows 2 (dashed line) and 3 (dotted line) of Figure 4 due to $\lambda_{probe} = 387.5$ nm for pure Kr, 20 K, and $\lambda_{pump} = 560$ nm. Window 2 is separated from window 3 by a change of fluorescence wavelength (Figure 4); for T_1 and T_2, see the text.

Next the dependence of $\nu(t)$ in the pump−probe spectra on sample temperature was studied, and an example is shown in Figure 6a) for 10 and 40 K with a pump wavelength of 580 nm ($E = 1841$ cm^{-1}). The temperature effect seems to be weak looking at one period, but it accumulates, and after 10 periods the oscillations are out of phase. The periods are shorter for 40 K, indicating that the wave packet arrives earlier at lower E values, i.e., an enlargened energy relaxation rate at high T. An increase of k_{en} with T is plausible because the increased amplitude in thermal oscillations of the matrix atoms causes a stronger interaction with the vibrational wave packet. The $d\nu/dt$ values at elevated temperatures relative to those at 10 K were combined with the known anharmonicity $(d\nu/dE)^{-1}$ for a quantitative evaluation. The resulting energy relaxation rate k_{en} for the first period is shown in Figure 5b. The decrease of dE/dt with E was taken into account for distributing the accumulated Δt value to the individual periods. The decrease in averaged intensity at 40 K relative to 10 K (Figure 6a) indicates that the wave packet passes more quickly through the probe window and illustrates once more the increased vibrational relaxation rate.

The I_2−Kr mixtures were codoped with a varying content of Ar. The I_2 molecule in a double-substitutional site of the matrix has 17 nearest neighbor host atoms in the fcc lattice of the rare gas. Thus, on average about 3−4 atoms in the surrounding cage are replaced by Ar for an Ar concentration around 20% of the Kr content. A comparison of the pump−probe spectrum in

Figure 6b for 20% Ar with that for 0% Ar demonstrates shorter vibrational periods for the Ar-doped samples which accumulate with t and lead to an out-off-phase oscillation after about six periods. The shortening of the vibrational period indicates once more an increase in k_{vib}. Ar concentrations of 3%, 10%, and 20% were studied, and the vibrational relaxation rate increases smoothly with doping. Doping the matrix has an effect similar to that of raising the matrix temperature, and it is even stronger. The enhanced vibrational relaxation is derived in the same way. The collection of the data from a systematic temperature and concentration study in Figure 5b confirms the increase in k_{en} with temperature and with Ar concentration.

The splitting of the first two oscillations for 0% Ar in Figure 6b originates from a passage of the wave packet through the probe window on the outward motion and once more after the turning point in the inward motion. The splitting gradually disappears with Ar concentration, indicating that the enhanced energy loss stops the wave packet already closer to the window. Thus, the outer bow becomes shorter, and the splitting is less pronounced. The enhanced energy relaxation also leads to a slight decay of the time-averaged amplitude for 20% Ar, with time, whereas it is constant for 0% Ar. This is in accord with the expectation that the wave packet falls partially out of the center of the probe window for the Ar doping.

It might be surprising that the modulation contrast is less damped for the Ar doping and oscillations up to 5 ps are visible (Figure 6b). The decay of the time-averaged amplitude and the modulation contrast are, however, strongly influenced by the position of the probe window relative to the center of the wave packet. This is clearly displayed for $\lambda_{probe} = 480$ nm in Figure 6c. The probe window is situated near the high-energy end of the wave packet. The time-averaged amplitude decays quickly because already a small energy loss scatters the wave packet out of the probe window. Thus, only that fraction with essentially no energy loss is recorded in Figure 6c, and this fraction keeps a deep modulation contrast up to more than 20 periods.

We attempted to probe the wave packet dynamics deeper in the B state through window 2 in Figure 4 with a probe wavelength of 387.5 nm. T_1 in Figure 6d corresponds to the round trip time for the first bow from the probe window to the outer turning point and back to the window. T_2 corresponds to the round trip time for the bow from the window to the inner turning point and back to the window. By recording the fluorescence at 408 or 426 nm, we switch from window 2 in Figure 4 with small R and small E to window 3 with larger R and larger E. The outer bow is longer for small R, and T_1 increases with window 2 compared to window 3. Thus, window 2 provides a possibility for probing the wave packet at low E. However, the signal rises for both spectra of Figure 6d after several picoseconds (not included in the figure). The rising contribution reflects the population accumulating in the A state by predissociation which is probed through window 4. The sensitivity for this transition is stronger, and an unambiguous deconvolution is difficult. Therefore, we were not able to monitor the wave packet dynamics up to the required later delay times.

6. Predissociation

The spectra in Figure 7a show the B state dynamics on a longer time scale of 50 ps probed through window 1 with $\lambda_{probe} = 456$ nm. The oscillations in the early part are hardly visible on this time scale, and here we focus on the decay of the signal

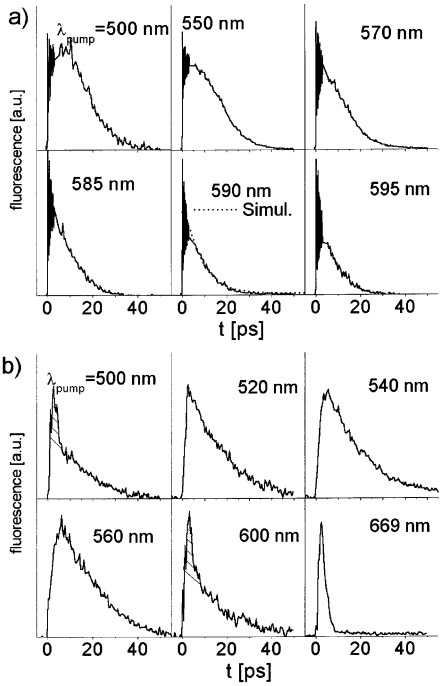

Figure 7. Same as Figure 6 on a longer time scale in pure Kr and at $T = 20$ K (oscillations not resolved). (a) Vibrational relaxation in the B state through window 1 (Figure 4) due to $\lambda_{probe} = 456$ nm. λ_{pump} is given in each panel. The dashed line is a simulation according to the text. (b) Predissociation leads to population in the A state which is recorded by window 4 (Figure 4) due to $\lambda_{probe} = 387.5$ nm and a fluorescence of 408 nm. For a discussion of the shaded part, see the text.

TABLE 2: Rise and Decay Times τ_1 and τ_2 from Figure 7b According to Eq 4[a]

T (K)	τ_1 (ps)	$\tau_2 = \tau_{pre}$ (ps)	k_{pre} (10^{-2} ps^{-1})	τ_B (ps)	τ_A (ps)
10	2 ± 1	17 ± 1	5.9 ± 0.4	8.6 ± 0.2	2.7
20	2 ± 1	14 ± 1	7.1 ± 0.6	7.6 ± 0.2	2.7
40	2 ± 1	9.5 ± 1	10.5 ± 1.1	6.0 ± 0.2	2.7

[a] $k_{pre} = 1/\tau_2$ represents the predissociation rate shown in Figure 10. τ_B is the decay time from Figure 7a. τ_A is the decay time for direct A excitation with 669 and 618 nm.

between about 10 and 50 ps. A monoexponential fit of the decaying wing yields a decay time $\tau_B = 7.6 \pm 0.2$ ps at 20 K for all pump wavelengths between 595 and 500 nm within the quality of the fit (Table 2). The decay time is, however, sensitive to the sample temperature (Figure 8a) and codoping with Ar (Figure 8b). The decay time shortens systematically with concentration and also with temperature (Figure 8c). The question is now to what extent this decay reflects vibrational energy relaxation in the B state through the probe window or depopulation of the B state by predissociation. There is a delay (Figure 7a) before the decay starts which increases systematically with shorter λ_{pump}, i.e., larger initial energy E. This constant ($\lambda_{pump} = 550$ nm) and even the rising part ($\lambda_{pump} = 500$ nm) clearly originate from energy relaxation. During this time the population relaxes from energies above the probe window into the window (optimal detection efficiency), and therefore, part of the decay also has to be attributed to this effect. To calibrate the sensitivity $S(\Delta E)$ versus energy difference ΔE to the center of the probe window, we kept the probe window fixed and shifted the initial energy up by shortening the pump wavelength. The decrease of signal with ΔE corrected for the change in absorption (Figure 2) and pump pulse intensity also yields the required sensitivity loss for a wave packet which relaxes out of

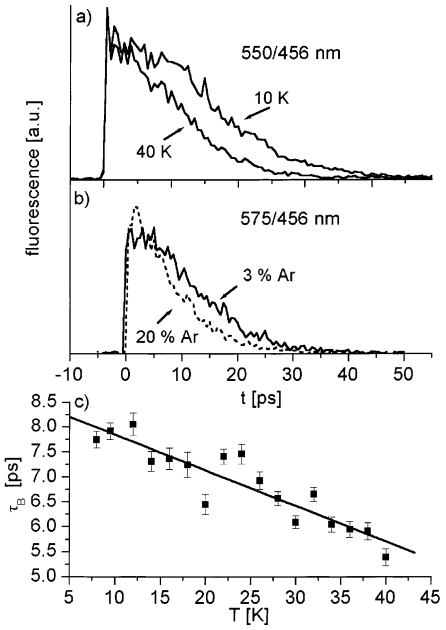

Figure 8. (a) Increase in vibrational relaxation in the B state from $T = 10$ K to $T = 40$ K recorded by window 1 ($\lambda_{probe} = 456$ nm) in pure Kr ($\lambda_{pump} = 550$ nm). (b) Similar increase by increasing additional doping with Ar from 3% to 20% relative to the Kr content of the matrix ($\lambda_{pump} = 575$ nm). (c) Decay time τ_B in the exponential wing of (a) for systematic variation of T.

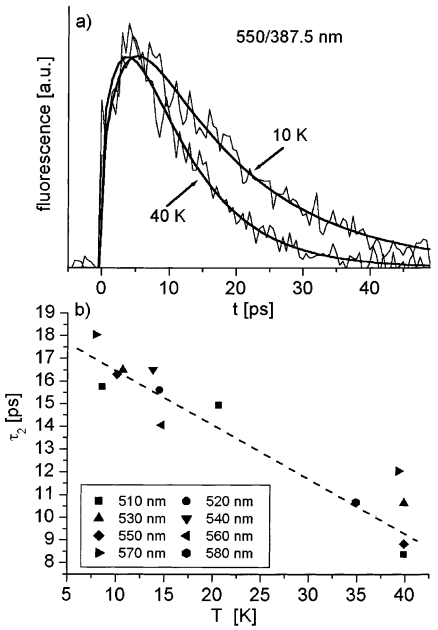

Figure 9. (a) Rise and decay of the transient population in the A state due to predissociation for $T = 10$ K and $T = 40$ K in pure Kr recorded by $\lambda_{probe} = 387.5$ nm through window 4 ($\lambda_{pump} = 550$ nm) and reproduced by eq 4 (solid lines) with fast component τ_1 and slow component τ_2. (b) Fitted slow component τ_2 versus T and a set of pump wavelengths given in the inset. The predissociation rate $k_{pre} = 1/\tau_2$ is obtained from τ_2.

the probe window. Using the known energy relaxation rate and $S(\Delta E)$, we can calculate the contribution to the decay in Figures 7 and 8 which results from vibrational energy relaxation k_{vib}. Of course the variation of k_{vib} with T and Ar concentration has to be included. The simulation for $\lambda_{pump} = 590$ nm is shown in Figure 7a. It agrees very well with the measured decay. Thus, most of the decay has to be attributed to the energy relaxation. The accuracy of the simulations is not sufficient to extract the weak predissociation part. Obviously, its contribution is definitely the smaller part, and hence, the predissociation time τ_{pre} is significantly longer than τ_B (Table 2): $\tau_{pre} > \tau_B$ at this probe window energy. Thus, already the lower limit for τ_{pre} (at the probe energy of 1500 cm^{-1} above the B minimum) given by τ_B is a factor of 2 larger than the value of 4.5 ps derived in ref 9, and our data yield an even larger difference to the high-pressure gas- and liquid-phase data.

Predissociation funnels the population into the A and A′ states, which can be probed via window 4 in Figure 4 and fluorescence at 408 nm (Figure 3). The time courses observed in window 4 on a long time scale of 50 ps are collected in Figure 7b. Direct excitation into the A state with $\lambda_{pump} = 669$ and 618 nm (not shown) yields the well-known A state wave packet dynamics and a decay with a time constant of $\tau_A = 2.7$ ps (Table 2), reflecting the relaxation of the A state wave packet out of the probe window. Next we monitor the population of the A state by excitation of the B state and subsequent predissociation. In fact for B state excitation ($\lambda_{pump} = 560-520$ nm in Figure 7b) we observe a quick rise on a 3 ps time scale and a decay with an about 15 ps decay constant. Using a two-step cascade model for feeding of A with rate k_2 and depopulation of the A state window region with rate k_1,[9] we obtain for the time course $N_A(t)$ of the A state window population

$$N_A \approx \frac{k_2}{k_2 - k_1}(e^{-k_1 t} - e^{-k_2 t}) \qquad (4)$$

The fit yields the times τ_1 and τ_2 corresponding to the rates k_1 and k_2, respectively. We observe one short component τ_1 between 1 and 3 ps and a long component τ_2 of about 17 ps for $T = 10$ K (Figure 9a and Table 2). The shorter time appears as the rise time and the longer time as the decay time in $N_A(t)$ of such a cascade independent of which one characterizes the population or the depopulation process. The prefactor $k_2/(k_2 - k_1)$ has to be the same for both exponentials. This condition was tested by a fit using two independent exponential functions and is very well fulfilled, and therefore, the use of eq 4 is justified. The depopulation time τ_A of the A state window agrees within the accuracy of the fit with the shorter time τ_1 (Table 2), and therefore, $\tau_1 = \tau_A$ represents the depopulation rate k_1. In this case $\tau_2 = 14$ ps for 20 K corresponds to the population time and thus to the feeding time of the A state. The measured rate $k_2 = 0.07$ ps^{-1} at 20 K contains two steps: the predissociation time for the B state and the time for transfer of population from the repulsive states (a, a′, B″, ...) to the lower lying A and A′ states. Thus, τ_2 is an upper limit for τ_{pre}, and k_2 is a lower limit for k_{pre} accordingly. To obtain information about population transfer from repulsive states to A and A′, we take a closer look at the measured spectra probed in the A or A′ state while exciting the B″ state, which is repulsive.

For $\lambda_{pump} = 600$ nm in Figure 7b we see a superposition of direct A state excitation with a 2.7 ps decay (shaded part) and the typical 14 ps (for $T = 20$ K, see Table 2) decay by B state predissociation. The superposition reflects the A and B state contribution in absorption (Figure 2). For $\lambda_{pump} = 500$ nm and also 480 nm (not shown) we see a similar superposition. In this case we get an increasing addition by B″ excitation (dashed) in accord with the absorption spectrum. B″ excitation leads to the same fast spike as direct A excitation. Obviously the repulsive B″ state feeds within 1 ps into the A or A′ state probe window. This also explains why the repulsive intermediate state in the B state predissociation does not show up in the B−A cascade explicitly. It hides behind the much longer predissociation time of typically 17 ps for 10 K.

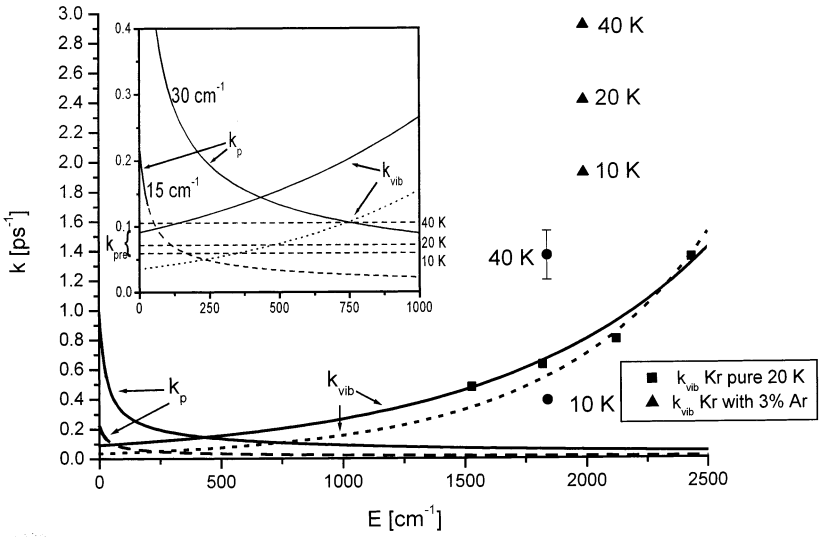

Figure 10. Similar to Figure 1. Predissociation rate $k_p(E)$ calculated according to ref 20 with $A = 30$ cm^{-1} (solid line) and 15 cm^{-1} (dashed line). The vibrational relaxation rate k_{vib} from an exponential extrapolation of the four new experimental data at 20 K (squares) is shown as a solid line and the dotted fit for all points in Figure 5a as a dotted line. The k_{vib} values for 10−40 K in pure Kr (closed circles) and for addition of 3% Ar (triangles) taken from Figure 5b are included. The inset shows the crossing region together with the new measured predissociation rates k_{pre} at 10, 20, and 40 K as horizontal dashed lines.

Therefore, we can neglect the rate for population transfer from repulsive states to our probe window. The measured rate k_2 corresponds to the predissociation rate $k_{pre} = k_2 = 0.07$ ps^{-1} at 20 K. It is essentially independent of the initial energy E in the B state (Figure 7b). However, it is increased by increasing the temperature (Table 2 and Figure 9b).

Our conclusion concerning the assignment of k_1 and k_2 to depopulation and population of the A state window is opposite to that in ref 9. There we did not recognize the quick A state dynamics for direct excitation, which led to the wrong interpretation. The times themselves agree with the present data.

For clarification, we sum up the experimental results concerning predissociation, before we combine those with the experimental results of vibrational relaxation in section 7, leading to a detailed rate model.

(1) Probing the B state at 1500 cm^{-1} above its minimum yields a decay of $\tau_B = 7.6 \pm 0.2$ ps at 20 K. The corresponding rate $k_B = 0.13$ ps^{-1} includes the rate for vibrational relaxation out of the probe window in B and for predissociation. The signal is reproduced within the experimental accuracy by just regarding the experimental data for vibrational relaxation (Figure 7a, 590 nm). Therefore, the predissociation rate at 1500 cm^{-1} has to be much smaller than $k_B = 0.13$ ps^{-1}.

(2) Direct A state excitation and A state probing (669 nm in Figure 7b) yield a prompt rise and a decay with $\tau_A = 2.7$ ps corresponding to a rate of 0.35 ps^{-1} (Table 2). τ_A is the vibrational cooling rate of the A state in the chosen probe window.

(3) On excitation of the B state and A or A′ state probing, we observe population in the A (or A′) state which has to result from predissociation (520, 540, and 560 nm in Figure 7b). Those signals show a quick rise with τ_A (from vibrational cooling in A or A′) and a long-living wing with a low rate constant $k_2 = 0.07$ ps^{-1}. k_2 is the feeding rate from B to the probe window in A or A′ at 20 K.

(4) k_2 represents a lower limit for the predissociation rate k_{pre} because it includes both k_{pre} and the rate for transfer from the repulsive states (a, a′, B″, ...), which cross B, to the probe window in A or A′.

(5) Excitation of the repulsive B″ state at 500 nm (and additional B) yields the same short spike as A excitation at 669 nm (see Figure 7b). It indicates that population transfer from repulsive states to the probe window used is fast compared to predissociation.

(6) Thus, k_2 is essentially the predissociation rate $k_{pre} = k_2 = 0.07$ ps^{-1} and not only its lower limit.

(7) τ_B and τ_{pre} are temperature dependent as listed in Table 2.

With the present analysis we arrive at a typical predissociation time of ∼17 ps, which is now a factor of 7 longer than that in ref 9, and the gap to the shorter liquid-phase and high-pressure data opens accordingly wider.

7. Discussion

7.1. Vibrational Relaxation. A comparison of the new results on the energy relaxation rate in Figure 5a with those of ref 9 shows a similar dependence on energy E, while the absolute values are somewhat higher due to the optimized choice of the probe wavelength.[31] The two points calculated by classical molecular dynamics[8] are in excellent agreement with the new experimental data. The data are now extended to smaller energies; however, it is still not possible to cover the most relevant range below $E < 1500$ cm^{-1}. Therefore, we have to rely on an extrapolation. The rather linear behavior over 2 orders of magnitude on the logarithmic plot of Figure 5a suggests an exponential extrapolation with a lower limit given by the dotted line and the best fit given by the solid line. We convert the dE/dt values from cm^{-1}/ps by division with ν_{osc} to vibrational relaxation rates k_{vib} in ps^{-1} as in Figure 1, and we present in Figure 10 the last experimental points (squares) at small E together with the dotted extrapolation from Figure 5 and an additional exponential fit (solid line), involving just the four data points of k_{vib} visible in Figure 10. We treat the dotted fit from Figure 5 as a lower estimate for k_{vib}, whereas the other extrapolation is considered an upper limit for k_{vib}. The solid line from Figure 5a lies between the two bonds. These systematic investigations on the energy dependence of k_{vib} were carried out for sample temperatures of 20 K. The variation of k_{vib} with T as depicted in Figure 5b is summarized by the filled circles for 10 and 40 K in Figure 10 after conversion of $k_{en} =$ dE/dt to k_{vib}. The increase of k_{vib} with Ar concentration is included in Figure 10 as triangles.

7.2. Predissociation. In analogy to Figure 1 we show the calculated predissociation rate $k_p(E)$ according to Nakamura et al.[20] with $V_{a-B} = 30$ cm^{-1} [11] as a solid line. In ref 12 a value of 14 cm^{-1} was obtained. Therefore, we include $k_p(E)$ for $V_{a-B} =$ 15 cm^{-1} for comparison (lower dashed line). In our model the crossing range of k_{vib} and k_p yields k_{equ} (Figure 1), the apparent predissociation rate. Therefore, this crossing range is shown on an enlarged scale in the inset of Figure 10. On this scale we summarize by the dashed horizontal lines the new results on the apparent predissociation rate $k_{pre} = 1/\tau_2$ from Figure 9b and Table 2. For the lowest temperature of approximately 10 K we obtain a predissociation time of 17 ps corresponding to $k_{pre} =$ 0.06 ps^{-1}. It increases to 0.07 and 0.11 ps^{-1} for 20 and 40 K, respectively. The new low-temperature k_{pre} is nearly 1 order of magnitude smaller than the 20 K rate of ref 9, which is not surprising due to the wrong interpretations of k_1 and k_2 in eq 3. It is, however, also a factor of 3 lower than that of ref 8. The improvement is mainly based on the separated determination of k_{vib} and k_{pre} in our case. Since the experimental predissociation rate k_{pre} is expected to be close to k_{equ} (Figure 1), it is possible to derive further restrictions for k_{vib} and k_p from the requirement of a consistency with k_{pre}. Obviously a combination of k_p for $V_{a-B} = 30$ cm^{-1} with the upper limit of the k_{vib} for 20 K extrapolation would lead to $k_{equ} = 0.14$ ps^{-1}, which is much too high compared to the new 20 K value of $k_{equ} = 0.07$ ps^{-1}. The crossing of k_p with $V_{a-B} = 15$ cm^{-1} and a k_{vib} extrapolation in the middle between the limits is in good agreement with k_{pre} at 20 K according to the inset in Figure 10.

7.3. Relation to B → X Emission. The experiments would be more conclusive if an excitation below and above E_{equ} would have been possible. E_{equ}, i.e., the energy for which k_p and k_{vib} coincide, lies around 230 cm^{-1} for $V_{a-B} = 15$ cm^{-1} and would shift to higher values for larger V_{a-B}. Additional information concerning E_{equ} is given by the hot B → A luminescence measured in the group of V. A. Apkarian.[10] It was possible to locate an energy region of about 700 cm^{-1} above the B state minimum from which the observed emission predominantly occurs in Xe and Kr matrixes. Using k_{vib} and k_p, we can calculate the transient distribution of energies E in the B state. Suppose we start high up in the B state with an energy E of several thousand inverse centimeters. The population relaxes quickly to E values around 1000 cm^{-1} due to the large k_{vib}, predissociation is slow, and the short transit time weakens radiative decay. Now on the way to E_{equ} the population piles up because k_{vib} slows down and k_p is still smaller than k_{vib}. The population which managed to pass E_{equ} will be damped progressively with time due to the dominating and increasing k_{pre}. Thus, this pileup of population at energies above but close to E_{equ} will be reflected in the radiative transition, and this range dominates the emission spectrum. This qualitative consideration is fully supported by the quantitative modeling of the emission spectra and is consistent with the derivation of the emission spectra in ref 10. Now we discuss the implications of the hot emission on the V_{a-B} value. A V_{a-B} value of 15 cm^{-1} leads to E_{equ} around 230 cm^{-1}, which is still consistent with a predominant emission from $E \approx 700$ cm^{-1}; however, it is already rather low. A further significant reduction of V_{a-B} would lead to a collapse of the transient population, too close to $E \approx 0$ to be consistent with the hot luminescence.

7.4. Effective Coupling Matrix Elements. A range of 15−20 cm^{-1} for V_{a-B} is rather likely for the low-temperature limit. This value is significantly smaller than the experimental result of 65 cm^{-1} from ref 8. The discrepancy arises mainly from our lower experimental k_{pre} and from the explicit inclusion of k_{vib}, which reduces E above the crossing. The discussion in ref 7 is rather detailed concerning the predictions using ref 15 (called the BC surface) and the predictions using ref 11 (called the RHB surface). Our new result is in rather good agreement with the RHB predictions, while, not surprisingly, the BC predictions for V_{a-B} now appear too large. The BC treatment was revised recently[17] and once more applied to solid Ar, leading to lower curve crossing probabilities at low T. The symmetry arguments are discussed, but the resulting effective values for the coupling matrix element are not given explicitly, and we cannot use them for comparison. A coupling between B and a′ dominates in ref 17. In this context we point out that our results are not specific concerning the dominant crossing, and the a state was taken as an example. From Figure 10 we in fact determine A in eqs 1 and 3. Thus, replacing F_a by the force F_x for another appropriate state x and keeping the same A leads to the matrix element V_{x-B} consistent with the experiment. The derived matrix element for a′ would be close to that for the a state, due to the similar $F_{a'}$.

7.5. Energy Flow and Disorder. The calculations for solid Ar were carried out for a pump wavelength of $\lambda_{pump} = 533$ nm, and a delay of 1.5 ps was observed (Figure 6, ref 17) before effective predissociation started. The delay was attributed to the required buildup of disorder by several collisions. The disorder should establish a sufficiently large coupling matrix element by removing the cancellation effects. Probing the B state dynamics in Figure 7a, we observe indeed a flat part on the order of 5−10 ps for excitation between 550 and 500 nm. This flat part originates, however, from vibrational relaxation to the energy of the probe window. A rather flat part of a few picoseconds can also be contained in the spectrum for $\lambda_{pump} =$ 540 nm in Figure 7b, which displays the predissociation dynamics. Once more this initial part, if discernible, reflects mainly the vibrational relaxation down to the region near E_{equ} where efficient predissociation is established by the proximity to the crossing. Predissociation itself takes place on a time scale of 16 ps, and it is unlikely that disorder initially created by large lattice amplitudes can be stored for such a long time.

Remember that for B state excitation near the gas-phase dissociation limit an energy of about 2000 cm^{-1} is distributed to the lattice in one vibrational period.[31] Lattice excitations are dissipated with high speed along densely packed crystal directions according to available calculations.[32−34] The speed of the first shock wave generated by I_2 in Kr was calculated explicitly to be 4.6 nm/ps.[34] Thus, this very fast heat flow is expected to cool the I_2 surroundings effectively on a time scale on which predissociation takes place (more than 10 ps!). The measured vibrational relaxation rate closest to the crossing of 0.5 ps^{-1} (at 1500 cm^{-1}) corresponds to an energy loss of only one vibrational quantum in 6−7 vibrational periods (one vibrational period at $E = 1500$ cm^{-1} in the B state is approximately 300 fs[31]). It diminishes furthermore as the population gets closer to the crossing. This explains why local heating by vibrational energy dissipation has a minor effect on predissociation. Therefore, the thermal heating of the matrix can generate the observed temperature effects. It is interesting to check how the measured signal loss in the B state window with $\tau_B = 7.6$ ps at $E = 1500$ cm^{-1} fits the survey of Figure 10. The rate k_{vib} is much larger than k_p at this energy. Therefore, the decay could be reproduced by vibrational relaxation only, without including k_{pre} (dashed line in Figure 7a, 590 nm).

We believe that more details on this interrelation of vibrational relaxation, predissociation, and disorder are contained in the calculated trajectories. The decrease in oscillation amplitudes with time in Figure 4 of ref 17 reflects, for example, the

vibrational relaxation history which then triggers predissociation. Therefore, an analysis of the trajectories directed at disentangling these processes may be very helpful.

7.6. Temperature Dependence of Predissociation. Next we turn to the temperature effects collected in Figure 10. A mild increase in k_{vib} and k_{pre} occurs by a temperature variation from 10 to 20 K. The jump to 40 K nearly doubles k_{pre}, and k_{vib} ($E = 1800$ cm^{-1}) triples. If k_{vib} in the crossing region increases by a factor of 2, it corresponds to the upper k_{vib} curve in the inset. In this case the higher lying crossing with k_p for $V_{a-B} = 15$ cm^{-1} accounts for the increase in k_{pre}. Thus, the temperature-induced stimulation of predissociation reflects mainly an acceleration in the vibrational relaxation. Disorder by Ar doping and also a combination of Ar doping with temperature rise systematically enlarges k_{vib} at $E = 2000$ cm^{-1} (Figure 10). Compared to 10 K an increase by a factor of 5 is observed. The expectation of a corresponding increase in k_{equ} with still fixed $V_{a-B} = 15$ cm^{-1} would, however, not be correct. The quantum mechanical solution[20] yields a maximal k_{equ} of about 0.22 ps^{-1} for $V_{a-B} = 15$ cm^{-1}. To reach the larger k_{equ} of the liquid phase at 300 K, it is necessary to enlarge V_{a-B} at least to 30 cm^{-1} as shown in Figure 10. Thus, for the strong disorder of the liquid phase an increase in V_{a-B} by weakening the cancellation effects in the summation of the angular terms has to be included. However, the dramatic increase in k_{vib} with T is also essential to funnel the population quickly enough into the crossing region where the predissociation can happen on a picosecond or even subpicosecond time scale. The largest k_{vib} values in Figure 5a correspond to the dissipation of several thousand inverse centimeters in one I_2 vibration. They are observed for large I−I elongation. At high T the vibrational amplitudes of the matrix atoms reach a similar size. The matrix atoms can approach in their statistical motion the expanding I_2 molecule already during the first elongation period. Therefore, k_{vib} can become sufficiently large to support the very early predissociation seen in the liquid.

Acknowledgment. We thank N. Yu and Profs. A. Apkarian and D.F. Coker for intense communication on the predissociation dynamics, a reviewer for suggesting clarifications, and J. Piel and J. Pietzner for support in the NOPA installation. This work was funded by the Deutsche Forschungsgemeinschaft (DFG) within SFB 450.

References and Notes

(1) Frank, J.; Rabinowitch, E. *Trans. Faraday Soc.* **1934**, *30*, 120.
(2) Harris, A.; Brown, J.; Harris, C. *Annu. Rev. Phys. Chem.* **1988**, *39*, 341.
(3) Lienau, C.; Zewail, A. H. *J. Phys. Chem.* **1996**, *100*, 18629−18649.
(4) Materny, A.; Lienau, C.; Zewail, A. H. *J. Phys. Chem.* **1996**, *100*, 18650−18665.
(5) Liu, Q.; Wan, C.; Zewail, A. H. *J. Phys. Chem.* **1996**, *100*, 18667−18682.
(6) Scherer, N. F.; Jonas, D. M.; Fleming, G. R. *J. Chem. Phys.* **1993**, *99*, 153−168.
(7) Zadoyan, R.; Sterling, M.; Ovchinnikov, M.; Apkarian, V. A. *J. Chem. Phys.* **1997**, *107*, 8446.
(8) Zadoyan, R.; Sterling, M.; Apkarian, V. A. *J. Chem. Soc., Faraday Trans.* **1996**, *92*, 1821−1829.
(9) Bargheer, M.; Dietrich, P.; Donovang, K.; Schwentner, N. *J. Chem. Phys.* **1999**, *111*, 8556−8564.
(10) Almy, J.; Kizer, K.; Zadoyan, R.; Apkarian, V. A. *J. Phys. Chem.* **2000**, *104*, 3508−3520.
(11) Roncero, O.; Halberstadt, N.; Beswick, J. A. *J. Chem. Phys.* **1996**, *104*, 7554.
(12) Roncero, O.; Halberstadt, N.; Beswick, J. Caging and Nonadiabatic Electronic Transitions in I_2-M Complexes. In *Reaction Dynamics in Clusters and Condensed Phases*; Jortner, J., Levine, R., Pullman, B., Eds.; Kluwer Academic Publishers: Dordrecht, The Netherlands, 1993.
(13) Ben-Nun, M.; Levine, R. D.; Flemming, G. *J. Chem. Phys.* **1996**, *105*, 3035.
(14) Batista, V. S.; Coker, D. F. *J. Chem. Phys.* **1996**, *105*, 4033−4054.
(15) Batista, V. S.; Coker, D. F. *J. Chem. Phys.* **1997**, *106*, 6923−6941.
(16) Buchachenko, A.; Stepanev, N. *J. Chem. Phys.* **1996**, *104*, 9913.
(17) Yu, N.; Margulis, C. J.; Coker, D. F. *J. Chem. Phys. B* **2001**, *105*, 6728.
(18) Zener, C. *Proc. R. Soc. London, A* **1932**, *137*, 696.
(19) Ermoshin, V. A.; Engel, V. *Chem. Phys. Lett.* **2001**, *336*, 262−267.
(20) Zhu, C.; Nakamura, H. *J. Chem. Phys.* **1994**, *101*, 10630.
(21) Zhu, C.; Nakamura, H. *J. Chem. Phys.* **1995**, *102*, 7448.
(22) Landau, L. D.; Lifschitz, E. M. *Lehrbuch der Theoretischen Physik*; Quantenmechanik Verlag Harri Deutsch: Frankfurt, 1990; Vol. III.
(23) Batista, V.; Coker, D. Private communication.
(24) Helbing, J.; Chergui, M. *J. Chem. Phys.* **2001**, *115*, 6158.
(25) Wilhelm, T.; J.Piel,; Riedle, E. *Opt. Lett.* **1997**, *22*, 1494−1496.
(26) Bargheer, M.; Pietzner, J.; Dietrich, P.; Schwentner, N. *J. Chem. Phys.* **2001**, *115*, 9827.
(27) Tellinghuisen, J. *J. Chem. Phys.* **1982**, *76*, 4736−4744.
(28) Ovchinnivkov, M.; Apkarian, V. *J. Chem. Phys.* **1997**, *106*, 5775.
(29) Grzybowski, J. M.; Andrews, L. *J. Raman Spectrosc.* **1975**, *4*, 99−113.
(30) Huber, K. P.; Herzberg, G. *Molecular Spectra and Molecular Structure IV. Constants of Diatomic Molecules*; Van Nostrand Reinhold Co.: New York, 1979.
(31) Bargheer, M.; Gühr, M.; Dietrich, P.; Schwentner, N. *Phys. Chem. Chem. Phys.* **2002**, *4*, 75−81.
(32) Cenian, A.; Gabriel, H.; Hennig, S. *J. Tech. Phys. (Warsaw)* **1996**, *37*, 4173.
(33) Zadoyan, R.; Li, Z.; Martens, C. C.; Apkarian, V. A. *J. Chem. Phys.* **1994**, *101*, 6648.
(34) Borrmann, A.; Martens, C. C. *J. Chem. Phys.* **1995**, *102*, 1905.